Single-phase FeMnNiAl Compositionally Complex Alloy

Mohammed Hussien*and Vladimir Vishnyakov

Centre for Engineering Materials, University of Huddersfield, HD1 3DH, UK

Abstract

FeMnNiAl, a compositionally complex alloy, is close to having an equimolar composition and was prepared in bulk and thin-film forms. Arc melting under argon was used for bulk form preparation. The thin-film alloy was produced by Ion Beam Sputter Deposition on a silicon substrate at 620 K. X-Ray Diffraction (XRD) and Transmission Electron Microscopy (TEM) we used to assess the material crystallinity. Both forms display a single-phase with near equimolar composition and are in a single crystalline state. The material has a BCC structure with the lattice constant at 4.08 Å. Dark field TEM imagery reveals material nanotexturing in thin films. The potentiodynamic polarisation in 0.6 moles NaCl and H_2SO_4 shows that open circuit potential (against saturated calomel electrode) at room temperature is approximately -0.21 V. The HEA thin-film is demonstrated to be nobler than 304 SS as shown by the corrosion potential (by approximately 0.1V) and passivation layer development in the corrosive solutions. Nanoindentation test shows that FeMnNiAl alloy thin film has high hardness at 11.7 GPa. It is anticipated that high hardness combined with the passivation ability can make the FeMnNiAl alloy coating a viable candidate for protection of metallic constructions in corrosive environments

Keywords

FeMnNiAl, highly concentrated alloy, HEA, single-phase, thin film, corrosion resistance, hardness, Young's modulus

*) Corresponding author: Mohammed Hussein, Mohammed.Hussien@hud.ac.uk, tel. +44 1484 472 164

Introduction

Alloy needs to satisfy many requirements before it can be used in industry. Traditional performance-application-lifespan-price paradigm has been recently expanded to contain recyclability and sustainability. Many different in-service factors affect conventional alloys and their mechanical properties. Insufficient high-temperature stability for instance can lower the mechanical properties and corrosion resistance [1]. All alloys are multicomponent systems and should to stay in the pre-defined state at the in-service conditions. In broad terms, this only can be provided either by an alloy being in the thermodynamic equilibrium or by the high activation energy if evolution (e.g. phase separation) processes. As thermally activated processes are always present the materials in thermodynamic equilibrium are much more preferred if attainable solution.

While the lifespan of the engineering item is limited by many factors, the corrosion process remains one of the most important for many applications. Many corrosion-resistant materials have been developed but the corrosion resistance comes at a price. It is economically prudent to use surface protection thin-films on a generally structurally sound by cheaper and corrosively inferior material.

Alloying elements modify alloy properties and in-service behaviour. This follows the classical model when composition and structure come together to underpin material survival during in-service conditions. It was realised relatively recently that combining elements in high concentrations can lead to further properties' enhancements. The most basic phenomena, like entropy, can rise to play a significant role and enhance material engineering value.

High Entropy Alloys (HEAs) were initially defined as alloys that contain about five or more elements in equal or near-equiatomic concentrations [2-4]. Generally, the entropy effect manifests itself more and increases with the rise of the number of elements mixed. The maximum effect is observed at the element uniform molarity but noticeable positive effects can be achieved with less than five elements and elemental concentration from 5 to 35 at. % [5-10]. It can be found that an alloy is regarded as a HEA by many when it contains a few minor elements in concentrations less than 5 at. % [11].

HEAs attracted considerable attention due to their unique, in some cases tuneable, properties and microstructure [12-15]. The alloys have opened new application areas owing to their high hardness [12, 16], good thermal stability[17], good corrosion resistance [9, 18, 19] and high wear-resistance [20].

Far from all elemental metal mixtures produce single-phase HEAs. The overall picture is complex, as only some compositions tend to form a simple solid solution with a single-face-centred cubic (FCC), body-centred cubic (BCC) or hexagonal close-packed (HCP) structures. For example, five-component Fe20Cr20Mn20Ni20Co20 alloy forms a single FCC solid solution and solidifies dendritically [21]. Majority of so claimed HEAs form phase and element segregated materials, essentially they are but a multi-phase alloy[12, 22-27]. While numerous studies focus on single-phase solid solutions, two-phases and multi-phases alloys have demonstrated a useful set of properties too[28, 29]. An absence of a single-phase can make an alloy less attractive for some applications as it indicates potential thermodynamic instability.

The corrosion resistance of alloys relays on elements such as Al, Si, Cr and Ni, to name a few when these elements create passive protection films on the surface. The passivation film delays

or stops further corrosion underneath[30]. It should be stated clearly that the nature and behaviour of protective films always depend on corrosion media and overall thermodynamical conditions. HEAs, like many other alloys, demonstrate high corrosion resistance in many challenging environments, for instance, such as HCl and H_2S_4 acids [31]. It was shown, for example, that CuCrFeNiMn and NiCoCrFeMnCuC HEAs have good corrosion resistance to H_2S_4 at room temperature [32]. Furthermore, the corrosion resistance of Cu0.5NiAlCoCrFeSi is much better than for conventional 304-stainless steel in some conditions[12].

As HEAs demonstrate such attractive engineering properties it would be beneficial to use them as coating materials. Besides, it is better to use the HEAs as coating materials rather than use them as bulk materials so that one can have their excellent properties and keep the costs low [33]. Therefore, a lot of HEAs coatings in recent years have been investigated. Many coating deposition techniques such as plasma cladding [34], laser cladding [35, 36], plasma spraying and magnetron sputtering [37-39] are utilised.

Hydrocarbon, oil and gas, recovery inevitably brings some dissolved mineral water solutions so named connate water [40]. The solutions are effective electrolytes and readily interact with all surfaces in contact leading to corrosion. The emblematic approach then is to use alloys with high corrosion resistance, typically an alloy with a high content of Cr and/or Ni. Most recent review of the corrosion processes at hydrocarbon recovery and corrosion-resistant materials was produced by Popoola *et al.*[41]. It is obvious that the corrosion and overall structural material deterioration, fatigue cracking, for instance, are not limited to the surface and many materials weakening processes are closely linked to the surface properties. Surface coating with the high corrosion-resistant material with good mechanical properties is but one possible approach to address material problems in hydrocarbon recovery.

Both, traditional alloys and HEA usually contain many elements. This makes high-performance alloys complex in production and relatively expensive. Yet, as always, cost reduction is continuously attractive. The aim of this study was to synthesise a rather simple, with a limited number of abundant elements, alloy. The alloy was initially produced in bulk form by Vacuum Arc Melting and then as a thin-film by Ion Beam Sputter Deposition. During the arc melting process, the ingot cools relatively slowly. This provides significant time for the material to reach thermodynamical equilibrium and develop element segregation and phase separation if the material is inclined to do so. In thin-film deposition process, the thermodynamical state is expected to be further from the equilibrium point. This might have some benefits but the material properties can change over time.

The main aim of this study was to create a new HEA single phase material which is thermodynamically stable and has good protection properties as a thin film. We have created bulk material mostly to check thermodynamic stability towards phase segregation. The material electrochemical behaviour in acidic solutions and material mechanical properties such as hardness were investigated.

Experimental methods

The bulk alloys have been produced by Arc Melting furnace from a powder mixture of Fe, Mn, Ni and Al. The material purity was at the level of 99.9 %. The melts have been done in a

protective argon atmosphere (pressure at around 0.5 atm) and continued gas flow. The material was melted three times to guarantee chemical homogeneity and then allowed re-crystallisation. . This was done in accordance with multiple works on HEAs, see for example[12, 29, 42-44].

Ion beam sputter deposition system was described in detail in the earlier work, see for example [45]. For this work, combinations of Al, Fe, Mn, and Ni targets were used. The location of the targets was adjusted under sputtering argon ion beam so that the deposited film composition was close to equimolar. The substrate temperature was maintained at 620 K. The film thickness after two-hour deposition was at around 1.2 microns as measured by cross-sectioning.

In order to identify the crystalline phase, the X-Ray Diffraction (XRD) had been used. Transmission Electron Microscopy (TEM) sample was prepared by Focused Ion Beam (FIB) sectioning to assess the thin film structure. Energy Dispersive X-ray (EDX) analysis with ZAF correction in Field Emission Gun Scanning Electron Microscope (FEG SEM) was utilised for compositional analysis.

The materials corrosion properties were assessed by Potentiodynamic polarisation measurements. Three electrode cell was used with the material as the working electrode. Platinum counter electrode and saturated calomel reference electrode were employed as the reference electrode. The measurements were conducted in 0.6 moles NaCl and H_2SO_4 aerated solutions under atmospheric pressure and at room temperature. The electrolyte solutions were purged with nitrogen to remove the presence and effect of dissolved oxygen.

The polarisation scanning was done in line with the ASTM International (American Society for Testing and Materials) standard and the scanning rate was set close to 0.017 V/s [46]. Stainless Steel (304 SS) was used to compare corrosion properties. All materials were tested using the same standard parameters: the samples were kept in the cells for 600 s to stabilise Open Circuit Potential (OCP) and scanned between -0.1 and 1.2V against OCP with the scanning rate of 0.02 V/s.

In order to measure mechanical properties of the thin film, hardness and modulus were gauged by a nanoindentation. Berkovich indenter was used and the maximum load was set to 50mN so that only the thin-film properties are tested.

Results and discussion

Bulk samples were smelted at continuous argon flow under approximately one half of atmospheric pressure. The material ingots were polished and first examined by SEM (see Fig.1). Electron Backscatter Electron (BSE) image mode in Z (atomic mass) contrast setting was used in the first instance. The BSE imaging is very useful in this case as even not at the very high contrast setting it allows to see immediately if the atomic species are distributed uniformly or there is some element (phase) segregation. The BSE image is shown in Fig. 1a. The uniform grey contrast indicates that all elements in FeMnNiAl alloy are distributed uniformly and form a single phase. The EDX quantification data (see Table 1) demonstrate that the alloy has an equiatomic composition.

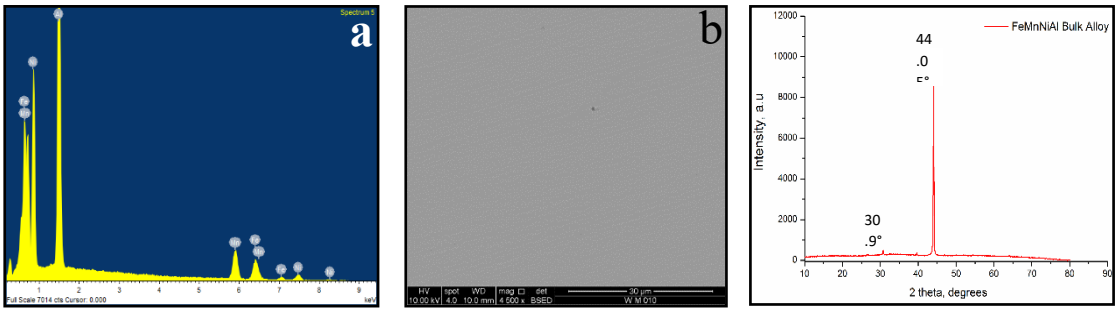

Figure 1. FeMnNiAl alloy HEA bulk alloy: a) - EDX spectra at 10 keV electron energy; b) – BSE surface image; c) – X-Ray Diffraction.

X-ray diffraction confirms that the alloy has a single phase with the main diffraction peak at 44.05˚ (see Fig.1c). The atomic structure corresponding to this diffraction pattern will be discussed later in this paper.

Data for the thin film FeMnNiAl HEA prepared by IBSD are presented in Fig 2 and Table 1. It can be seen that the film composition is very close to the bulk alloy and is also close to equiatomic. The X-ray diffraction pattern of the FeMnNiAl thin film has one high-intensity peak at 44.15˚ matchings with bulk alloy and the other low-intensity peak at 69.3˚ which is attributed to the silicon substrate.

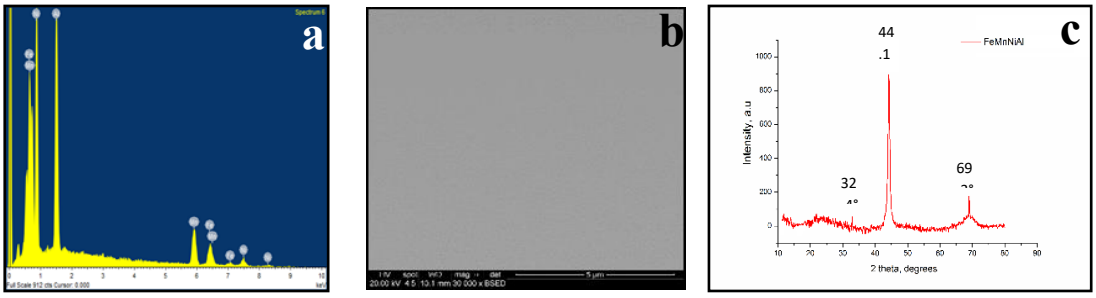

Figure 2. FeMnNiAl alloy HEA Thin Film alloy: a) - EDX spectra ay 10 keV electron energy. b) – BSE surface image; c) – X-ray Diffraction.

Table 1. Material Elemental Composition at 10 keV electron beam energy, ZAF correction, estimated error between 1.5-2 at.%.

Element	FeMnNiAl (Bulk alloy) atomic%	FeMnNiAl (Thin film) atomic%
Al K	24.4	23.4
Mn K	22.8	26.0
Fe K	25.5	26.3
Ni K	27.3	24.2

In both alloys, the EDX spectra show only surface related oxygen.

Further investigation of Crystalline structure of the FeMnNiAl HEA bulk sample was undertaken in Transmission Electron Microscope (TEM). The bright-field image (see Fig.3a) reveals some contrast variation within the film. The selected area diffraction demonstrates single-crystal structure which can be indexed as a BCC structure with the lattice constant at 4.08±0.016Å. The dark field image on (100) reflection shows nanostructured texturing. The nature of this texturing is unclear at the moment but it can be speculated that it is produced by the stochastical atomic composition variations during accommodation of atoms of different sizes and associated local stress. It is in line with the phenomena described earlier by Schwarzer [47] and need to be investigated further in our case.

Thin film was coated with the layer of Cr prior to lamellae cutting by Focused Ion Beam (FIB). Even bright-field image (see Fig.4a) in this case demonstrate nanocolumnar structure which is typical for thin film. Selected area diffraction reveals fine nanocrystalline structure. The structure is bordering on amorphous but with very small crystals. Dark field imaging from the highest intensity area in the diffraction ring reveals previously notices small crystallites textures along with pronounced columns. The nanocolumnar structure is, as was mentioned before, a distinctive attribute of thin-film growth. However, in the case of HEA alloy, the nanostructuring is most probably provided by the local stresses associated with the accommodation of atoms of different sizes.

It is plausible that the basic BCC structure in both, bulk and thin-film material, is the same but there is a variation, yet undetermined, in nano texturing, due to different sintering conditions (the temperature, cooling rate and stresses, to name just a few).

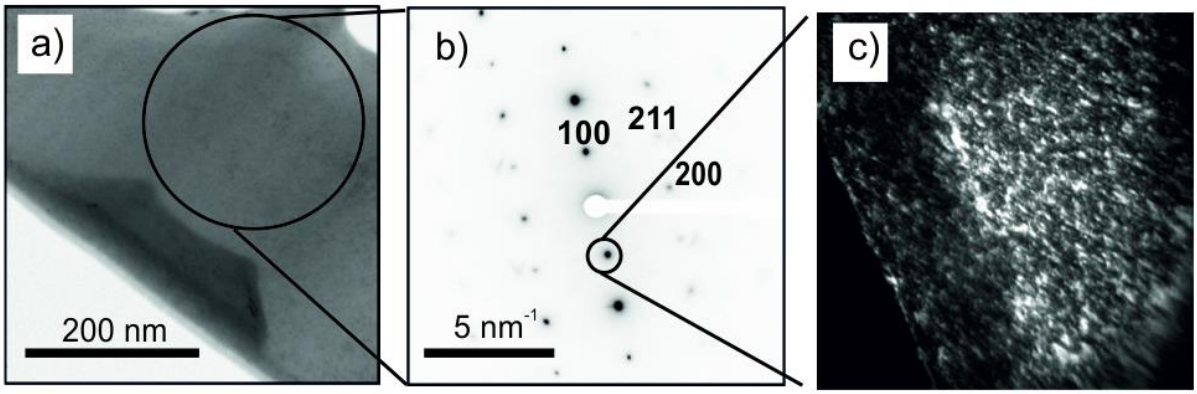

Figure 3. TEM data of lamellae from FeMnNiAl HEAbulk sample: a) – bright field image; b) – selected area diffraction; c) – dark field image.

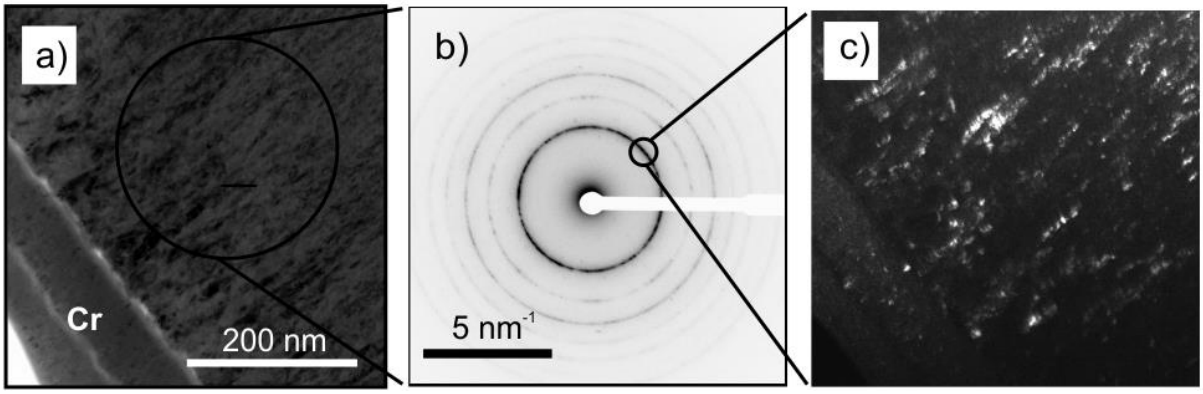

Figure 4. TEM data of lamellae from FeMnNiAl HEA thin film sample: a) – bright field image, b) – selected area diffraction from the thin film; c) – dark field image.

Potentiodynamic polarisation measurements were done in three-electrode electrochemical cell. The measurements were conducted in two different common test corrosive environments: NaCl and H_2SO_4 water solutions. The results for the HEA and 304SS shown in Figs 5 and 6.

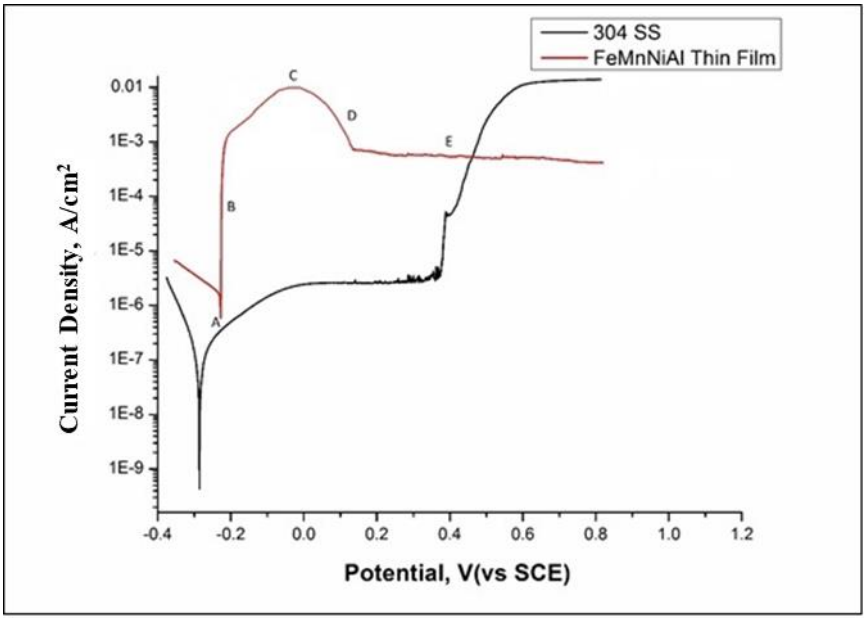

Figure 5- Potentiodynamic polarisation for 304SS and FeMnNiAl HEA thin-film in NaCl solution.

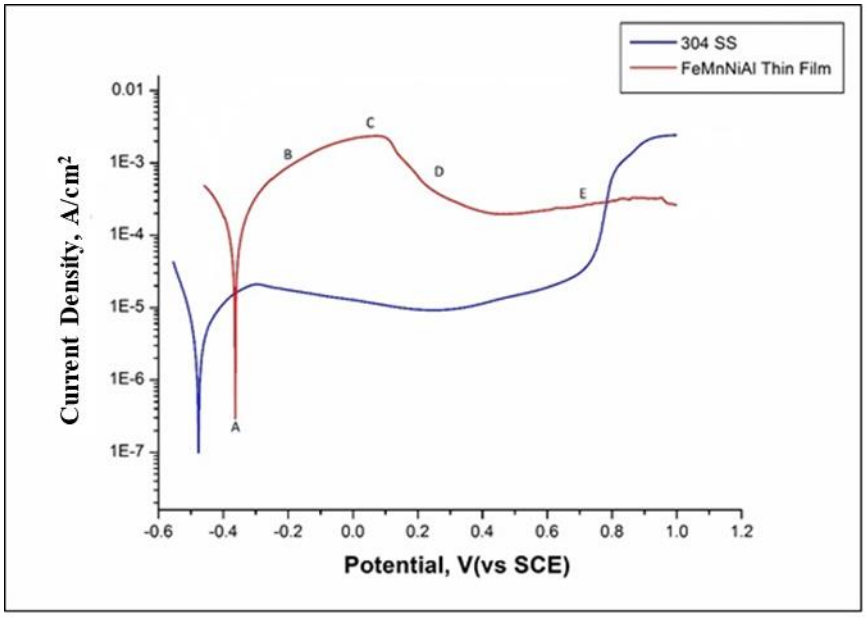

Figure6. Potentiodynamic polarisation for 304SS and FeMnNiAl thin HEA in H2SO4 solution.

Table2. Electrochemical parameters of 304SS and FeMnNiAl alloy thin-film in 0.6 moles NaCl and 0.6 moles H_2SO_4 at 25 °C.

Sample	**NaCl**		**H_2SO_4**	
	I_{corr}, A/cm²	**E_{corr}, V**	**I_{corr}, A/cm²**	**E_{corr}, V**
304 SS	8.3*E-9	-0.29	1.0*E-7	-0.48
FeMnNiAl	1.2*E-6	-0.22	6.0*E-6	-0.35

Nanoindentation.

The hardness measurements were done to the thin-film alloy. The indentation load has been gradually increased from 10 to 50 mN. As can be seen from the Fig.7 this allowed to probe up to approximately 1/3 of the film thickness. 1/3 can be regarded as an excessive penetration for the thin film properties measurement when usually 1/10 of thickness is probed. However, in this case, we need to remember that hardness of the silicon itself is at around 11 GPa [48] and the substrate, silicon, influence on film hardness measurement is absent. The dependence of film hardness on penetration depth was studied and no depth dependence was observed with higher penetration depth in our case. The film hardness was measured to be 11.7±0.65 GPa.

Young's modulus depends on the indentation depth (see Fig.8). According to the international standard, a Young's modulus value should be determined at zero load which is only possible by an approximation. Linear fit in our case produces value at around 197 GPa.

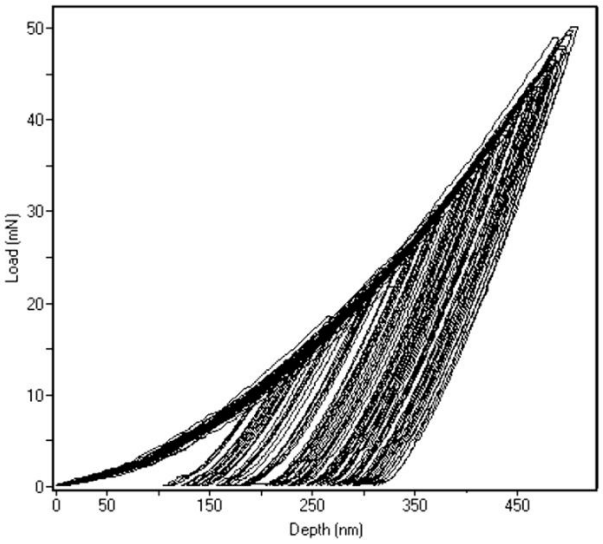

Figure 7. Nanoindentation data set for FeMnNiAl thin-film.

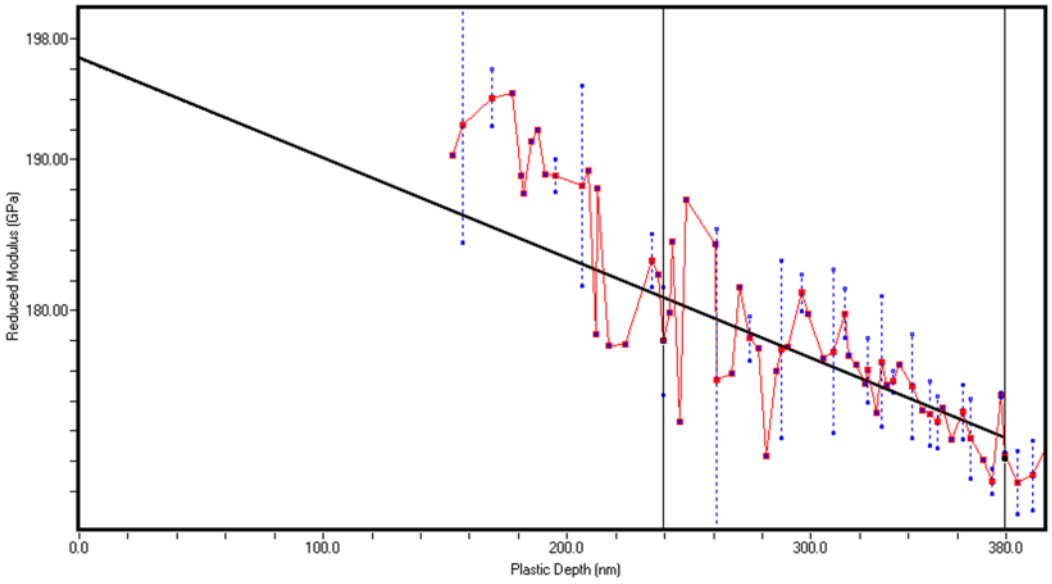

Figure 8. Reduced Young's the modulus over plastic depth for FeMnNiAl thin film.

Discussions

On the microscale (SEM images and EDX mapping) and nanoscale (XRD and TEM), the alloy has a single-phase and no visible element segregation. XRD diffraction from both materials shows similar XRD pattern which indicates that bulk and thin-film material are generally single-phase material which is in the same crystalline form. For the bulk alloy, the TEM data show well-formed BCC nanocrystals with the lattice parameter at 4.08±0.014 Å. There is also some nanotexturing. Thin-film demonstrates single-phase nanocolumnar structure which is usually associated with the Physical Vapor Deposition growth. In broad terms, this follows the well known Thorton's model [49]. In HEAs, the diffusion is known to be suppressed due to difference in atom sizes and this needs to be considered for analysis of thin-film growth [50].

There is a significant number of small nanocrystals bordering on the amorphous phase with random orientation in the thin film. However, the bigger nanocrystals appear to be well columnal texture aligned along the film growth direction. On the basis of very similar XRD pattern between bulk material and the thin-film, it is possible to assume that the crystalline structure is the same – BCC lattice. The calculated then lattice parameter is at 4.09±0.019 Å. The higher lattice error produced by bigger uncertainty in the parameter determination and also reflects on possible interatomic distances variation. It is also possible to see that XRD peak from the thin film is broader as compared to one from bulk material. At this point, we would refrain from using a very popular approach to employ the Scherrer approximation [51].

The reasons are twofold. Firstly, Scherrer approximation involves some assumptions which we cannot justify at the moment. Secondly, in our case, we can rely on dark field imaging for partial nanocrystal size assessment. Crystal size can be measured at different tilts. This is significant job by itself and need to be done separately. All the above requires an additional analysis which is outside of this work.

At the moment it is possible only to conclude that slightly bigger lattice constant in the thin film indicates that there is a possibility for further lattice relaxation for the thin-film. It is not surprising as the thin-films are not expected to be in the thermodynamical equilibrium. Most important at this time is that given chance to reach thermodynamical equilibrium during bulk sample cooling the material still remains in single-phase state.

Another significant fact is the prevailing nanocrystalline arrangements. TEM data demonstrate nano texturing in both cases. It is widely accepted that usually texturing is associated with some stress [52]. At the same time presence of impurities can also lead to nanostructuring [53]. It is not clear what is exactly mechanism leads to nanotexturing but nanotexturing is generally beneficial for the mechanical properties [50] and see later.

The stress influence on the structure for a different HEA in Ion Beam Sputter Deposition process was observed by us earlier [37]. It is impossible to establish an exact reason for the nanotexturing but work is underway to uncover the cause.

For the bulk alloy sample, the BSE image displays a uniform phase material with pores. The pores presence during arc melting is usually associated with trapped gases.

It is clear from the results for the bulk and thin-film samples that the alloy is stable in a relatively broad temperature range as otherwise, the structure would be different for bulk phase

which cools down from the melt much slower than the atoms during thin film growth. The alloy behaviour in broad terms should be understood from the atomic size of the elements, packing density and mixing entropy [54-56]. It has already been shown by many researchers that formation of a single-phase HEA by arc melting can only be achieved if the difference between atomic sizes is not too big ($\delta<8.6$). It is quite possible that in our case the alloy is on the verge of mismatch variation limit and this leads to stress and texturing. However, the mixing entropy is relatively high and only single phase is observed.

Electrochemical test.

From Tab.2 it is possible to see that the corrosion potential (E_{corr}) in NaCl for the HEA is -0.22 mV while the 304 Stainless Steel has corrosion potential at -0.29 V. The corrosion density (I_{corr}) of the FeMnNiAl is1.2E-6A/cm^2 which was higher than for SS (5.8E-8A/cm^2).

The SS in both solutions exhibits typical behaviour with broad passivation potential and then switch to pitting behaviour at pitting potential (Ep). In 304 SS case, an oxide layer starts to grow and protect the material until potential reaches about 0.4 volts then the oxide break down, which clear from the graph as the current density increased swiftly from 1E-5to 1E-2 A/cm^2.

In the FeMnNiAl case, the corrosion behaviour in chloride solution is quite different from 304 SS. The HEA is active at the beginning of positive polarisation but then current density saturates and even falls to a stable level. This behaviour indicates the establishment of passivation layer [46]. This layer grows on the surface and protects underlying. The passivation layer provides effective protection up to at least 0.9V. Up to this potential, there is no pitting. It is not clear at the moment if the passivation layer corrosion current would be reduced if the polarization scan will be done at the slower speed. The304 SS in the polarisation beginning is more corrosion resistant compared to FeMnNiAl thin film alloy. However, at high polarisation voltages, the FeMnNiAl thin film alloy is more protective.

Material behaviour in 0.6 moles of H_2SO_4 generally repeats observation for the chloride solution with slightly different potentials. Again, higher oxidation activity of HEA at the beginning of polarisation is replaced with the growth of protective layer which then stabilises oxidation at least up to 1.0V.

In general, elements such as Al and Ni forming a passivation layer which improves the corrosion resistance of the alloy [57]. At the same time presence of aluminium was observed to increase corrosion current [58]. It is not clear at the moment how the deviation of aluminium content can affect the initial passivation activity and the oxide film behaviour. More studies with adjusted constituent are needed to investigate passivation in this system

Mechanical properties

The thin film hardness in the region of 11 GPa is not very high value compared to ceramics like carbides or nitrides [59, 60]when hardness reaches 30-40 GPa. However, considering that alloys are usually softer (M4 steel has hardness at around 4 GPa without additional hardening and contemporary nickel superalloys hardness is at around 9 GPa), the hardness is reasonably high.

Hardness is associated with dislocation generation, dislocation gliding and dislocation pinning.

It has been shown many times for various materials that nanostructuring does increase hardness [61]. Further hardness enhancement in our case can be also attributed to nanotexturing [62]. Additional hardness is known to be also produced by the solid-solution effect[63].

It is consequently reasonable to assume that FeMnNiAl high metallic alloy film high hardness is produced by the present random atomic mixture of the constituent atoms which are positioned in nanocrystalline BCC arrangement. The nano stress then leads to nanocrystal texturing and further enhances hardness by impeding dislocation gliding.

Conclusions

FeMnNiAl metallic alloy in close to equiatomic conditions was sintered by Arc melting and Ion beam sputter deposition. Both routes produce single BCC phase alloy material with a reasonably stable crystalline structure. Electrochemical data in chloride and sulphate solutions demonstrate that the alloy is nobler than the 304 SS. Initial electrochemical activity on the positive polarisation leads to the growth of protective oxide layer which then demonstrates a very high level of stability by the absent pitting up to cathodic potential in the region of at least 0.9V. This is a high passivation ability. The FeMnNiAl alloy has high hardness at 11.7 GPa which is provided by the atomic arrangements and nanostructuring. High hardness and the material metallic nature should provide high erosion resistance. Combination of erosion resistance and high corrosion resistance makes the FeMnNiAl alloy films a good candidate for metallic construction in oil and gas exploration.

Reference list

1. Wang, Y., et al., *Effect of sigma phase precipitation on the mechanical and wear properties of Z3CN20. 09M cast duplex stainless steel.* 2013. **259**: p. 1-7.
2. Yin, S., et al., *Deposition of FeCoNiCrMn high entropy alloy (HEA) coating via cold spraying.* 2019. **35**(6): p. 1003-1007.
3. Guo, S., et al., *Effect of valence electron concentration on stability of fcc or bcc phase in high entropy alloys.* 2011. **109**(10): p. 103505.
4. Miracle, D.B. and O.N.J.A.M. Senkov, *A critical review of high entropy alloys and related concepts.* 2017. **122**: p. 448-511.
5. Zhang, H., et al., *Synthesis and characterization of FeCoNiCrCu high-entropy alloy coating by laser cladding.* 2011. **32**(4): p. 1910-1915.
6. Lee, C., et al., *Enhancing pitting corrosion resistance of AlxCrFe1. 5MnNi0. 5 high-entropy alloys by anodic treatment in sulfuric acid.* 2008. **517**(3): p. 1301-1305.
7. Yeh, J.-W., et al., *Formation of simple crystal structures in Cu-Co-Ni-Cr-Al-Fe-Ti-V alloys with multiprincipal metallic elements.* 2004. **35**(8): p. 2533-2536.
8. Huang, Y.-S., et al., *Microstructure, hardness, resistivity and thermal stability of sputtered oxide films of AlCoCrCu0. 5NiFe high-entropy alloy.* 2007. **457**(1-2): p. 77-83.
9. Tung, C.-C., et al., *On the elemental effect of AlCoCrCuFeNi high-entropy alloy system.* 2007. **61**(1): p. 1-5.
10. Huang, P.K., et al., *Multi-principal-element alloys with improved oxidation and wear resistance for thermal spray coating.* 2004. **6**(1-2): p. 74-78.
11. Tsai, M.-H. and J.-W.J.M.R.L. Yeh, *High-entropy alloys: a critical review.* 2014. **2**(3): p. 107-123.
12. Zhang, Y., et al., *Microstructures and properties of high-entropy alloys.* 2014. **61**: p. 1-93.
13. Ma, D., et al., *Correlation between glass formation and type of eutectic coupled zone in eutectic alloys.* 2003. **44**(10): p. 2007-2010.
14. Senkov, O.N., et al., *Mechanical properties of Nb25Mo25Ta25W25 and V20Nb20Mo20Ta20W20 refractory high entropy alloys.* 2011. **19**(5): p. 698-706.
15. Li, C., et al., *Effect of alloying elements on microstructure and properties of multiprincipal elements high-entropy alloys.* 2009. **475**(1-2): p. 752-757.
16. Gao, M.C., et al., *High-entropy alloys: fundamentals and applications*. 2016: Springer.
17. Tong, C.-J., et al., *Microstructure characterization of Al x CoCrCuFeNi high-entropy alloy system with multiprincipal elements.* 2005. **36**(4): p. 881-893.
18. Kao, Y.-F., et al., *Microstructure and mechanical property of as-cast,-homogenized, and-deformed AlxCoCrFeNi (0≤ x≤ 2) high-entropy alloys.* 2009. **488**(1): p. 57-64.
19. Chen, S.-T., et al., *Microstructure and properties of age-hardenable AlxCrFe1. 5MnNi0. 5 alloys.* 2010. **527**(21-22): p. 5818-5825.
20. Wang, F., Y.J.M.S. Zhang, and E. A, *Effect of Co addition on crystal structure and mechanical properties of Ti0. 5CrFeNiAlCo high entropy alloy.* 2008. **496**(1-2): p. 214-216.
21. Cantor, B., et al., *Microstructural development in equiatomic multicomponent alloys.* 2004. **375**: p. 213-218.
22. He, J., et al., *Effects of Al addition on structural evolution and tensile properties of the FeCoNiCrMn high-entropy alloy system.* 2014. **62**: p. 105-113.
23. Yeh, J.W., et al., *Nanostructured high-entropy alloys with multiple principal elements: novel alloy design concepts and outcomes.* 2004. **6**(5): p. 299-303.
24. Youssef, K.M., et al., *A novel low-density, high-hardness, high-entropy alloy with close-packed single-phase nanocrystalline structures.* 2015. **3**(2): p. 95-99.
25. Gludovatz, B., et al., *A fracture-resistant high-entropy alloy for cryogenic applications.* 2014. **345**(6201): p. 1153-1158.
26. Zhao, Y., et al., *A hexagonal close-packed high-entropy alloy: The effect of entropy.* 2016. **96**: p. 10-15.

27. Seifi, M., et al., *Fracture toughness and fatigue crack growth behavior of as-cast high-entropy alloys.* 2015. **67**(10): p. 2288-2295.
28. Miracle, D.J.M.S. and Technology, *Critical assessment 14: High entropy alloys and their development as structural materials.* 2015. **31**(10): p. 1142-1147.
29. Xiao, D., et al., *Microstructure, mechanical and corrosion behaviors of AlCoCuFeNi-(Cr, Ti) high entropy alloys.* 2017. **116**: p. 438-447.
30. Shi, Y., B. Yang, and P.J.M. Liaw, *Corrosion-resistant high-entropy alloys: A review.* 2017. **7**(2): p. 43.
31. Chen, Y., et al., *Microstructure and electrochemical properties of high entropy alloys—a comparison with type-304 stainless steel.* 2005. **47**(9): p. 2257-2279.
32. Florea, I., et al. *Study on corrosion resistance of high-entropy alloy in medium acid liquid and chemical properties*. in *IOP Conference Series: Materials Science and Engineering*. 2015. IOP Publishing.
33. Shon, Y., et al., *Laser additive synthesis of high entropy alloy coating on aluminum: Corrosion behavior.* 2015. **142**: p. 122-125.
34. Lu, J., et al., *Microstructure evolution and properties of CrCuFexNiTi high-entropy alloy coating by plasma cladding on Q235.* 2017. **328**: p. 313-318.
35. Shu, F., et al., *Structure and high-temperature property of amorphous composite coating synthesized by laser cladding FeCrCoNiSiB high-entropy alloy powder.* 2018. **731**: p. 662-666.
36. Ley, N., et al., *Laser coating of a CrMoTaWZr complex concentrated alloy onto a H13 tool steel die head.* 2018. **348**: p. 150-158.
37. Tunes, M.A., V.M. Vishnyakov, and S.E.J.T.S.F. Donnelly, *Synthesis and characterisation of high-entropy alloy thin films as candidates for coating nuclear fuel cladding alloys.* 2018. **649**: p. 115-120.
38. Zhang, W., et al., *Preparation, structure, and properties of an AlCrMoNbZr high-entropy alloy coating for accident-tolerant fuel cladding.* 2018. **347**: p. 13-19.
39. Cao, F., et al., *Microstructure and mechanical properties of a multilayered CoCrNi/Ti coating with varying crystal structure.* 2018. **350**: p. 596-602.
40. Vishnyakov, V., et al., *Primer on Enhanced Oil Recovery*. 2019: Gulf Professional Publishing 222.
41. Popoola, L.T., et al., *Corrosion problems during oil and gas production and its mitigation.* 2013. **4**(1): p. 35.
42. Shi, Y., et al., *Corrosion of Al xCoCrFeNi high-entropy alloys: Al-content and potential scan-rate dependent pitting behavior.* 2017. **119**: p. 33-45.
43. Senkov, O., et al., *Refractory high-entropy alloys.* 2010. **18**(9): p. 1758-1765.
44. Santodonato, L.J., et al., *Deviation from high-entropy configurations in the atomic distributions of a multi-principal-element alloy.* 2015. **6**: p. 5964.
45. Vishnyakov, V., et al., *Amorphous Boron containing silicon carbo-nitrides created by ion sputtering*. Surface and Coatings Technology, 2011. **206**: p. 149-154.
46. Enos, D. and L. Scribner, *The Potentiodynamic Polarisation Scan–Technical Report 33.* Solartron Instruments, 1997.
47. Schwarzer, R., *The determination of local texture by electron diffraction–a tutorial review.* Textures and Microstructures, 1970. **20**.
48. Ericson, F., S. Johansson, and J.-Å. Schweitz, *Hardness and fracture toughness of semiconducting materials studied by indentation and erosion techniques.* Materials Science and Engineering: A, 1988. **105**: p. 131-141.
49. Thornton, J.A., *Influence of apparatus geometry and deposition conditions on the structure and topography of thick sputtered coatings.* Journal of Vacuum Science and Technology, 1974. **11**(4): p. 666-670.
50. Tunes, M.A. and V.M. Vishnyakov, *Microstructural origins of the high mechanical damage tolerance of NbTaMoW refractory high-entropy alloy thin films.* Materials & Design, 2019. **170**: p. 107692.

51. Scherrer, P., *Bestimmung der inneren Struktur und der Größe von Kolloidteilchen mittels Röntgenstrahlen*, in *Kolloidchemie Ein Lehrbuch*. 1912, Springer. p. 387-409.
52. Šiška, F., S. Forest, and P. Gumbsch, *Simulations of stress–strain heterogeneities in copper thin films: Texture and substrate effects.* Computational Materials Science, 2007. **39**(1): p. 137-141.
53. Braeckman, B., et al., *Impurity-controlled film growth and elastic properties of CoCrCuFeNi thin films.* Surface and Coatings Technology, 2017. **315**: p. 475-483.
54. Ye, Y., et al., *The generalized thermodynamic rule for phase selection in multicomponent alloys.* 2015. **59**: p. 75-80.
55. Ye, Y., et al., *High-entropy alloy: challenges and prospects.* 2016. **19**(6): p. 349-362.
56. Sheng, G. and C.T.J.P.i.N.S.M.I. Liu, *Phase stability in high entropy alloys: formation of solid-solution phase or amorphous phase.* 2011. **21**(6): p. 433-446.
57. Soare, V., et al., *Influence of remelting on microstructure, hardness and corrosion behaviour of AlCoCrFeNiTi high entropy alloy.* Materials Science and Technology, 2015. **31**(10): p. 1194-1200.
58. Lee, C., et al., *Effect of the aluminium content of AlxCrFe1. 5MnNi0. 5 high-entropy alloys on the corrosion behaviour in aqueous environments.* Corrosion Science, 2008. **50**(7): p. 2053-2060.
59. Beake, B., V. Vishnyakov, and A. Harris, *Relationship between mechanical properties of thin nitride-based films and their behaviour in nano-scratch tests.* Tribology International, 2011. **44**(4): p. 468-475.
60. Popov, O., S. Chornobuk, and V. Vishnyakov, *Structure formation of TiB2-TiC-B4C-C hetero-modulus ceramics via reaction hot pressing.* International Journal of Refractory Metals and Hard Materials, 2017. **64**: p. 106-112.
61. Semenova, I.P., et al., *Ultrafine-Grained Titanium-Based Alloys: Structure and Service Properties for Engineering Applications.* Advanced Engineering Materials, 2020. **22**(1): p. 1900651.
62. Vázquez Martínez, J.M., et al., *Effects of laser processing parameters on texturized layer development and surface features of Ti6Al4V alloy samples.* Coatings, 2018. **8**(1): p. 6.
63. Zhang, W., et al., *Preparation, structure, and properties of an AlCrMoNbZr high-entropy alloy coating for accident-tolerant fuel cladding.* Surface and Coatings Technology, 2018. **347**: p. 13-19.